IEEE Access
Multidisciplinary ⋮ Rapid Review ⋮ Open Access Journal

Received 22 November 2022, accepted 9 December 2022, date of publication 15 December 2022,
date of current version 21 December 2022.

Digital Object Identifier 10.1109/ACCESS.2022.3229590

RESEARCH ARTICLE

CMA-Based Four-Element Broadband Circularly Polarized Octagonal-Ring Slot Antenna Array for S-Band Satellite Applications

NATHAPAT SUPREEYATITIKUL[1], TITIPONG LERTWIRIYAPRAPA[2], (Senior Member, IEEE), MONAI KRAIRIKSH[3], (Senior Member, IEEE), AND CHUWONG PHONGCHAROENPANICH[3], (Member, IEEE)

[1]Aeronautical Engineering Division, Civil Aviation Training Center, Bangkok 10900, Thailand
[2]Research Center of Innovation Digital and Electromagnetic Technology (iDEMT), Department of Teacher Training in Electrical Engineering, Faculty of Technical Education, King Mongkut's University of Technology North Bangkok, Bangkok 10800, Thailand
[3]School of Engineering, King Mongkut's Institute of Technology Ladkrabang, Bangkok 10520, Thailand

Corresponding author: Chuwong Phongcharoenpanich (chuwong.ph@kmitl.ac.th)

This work was supported in part by the King Mongkut's Institute of Technology Ladkrabang under Grant 2565-02-01-098; in part by the National Science, Research and Innovation Fund (NSRF); and in part by the King Mongkut's University of Technology North Bangkok under Contract KMUTNB-FF-66-48.

ABSTRACT This research proposes a low-complexity and low-profile four-element circularly polarized (CP) octagonal-ring slot antenna array with sequentially-rotated feed network for S-band satellite applications. The proposed antenna array is characterized by characteristic mode analysis (CMA). One single element of the CP octagonal-ring slot antenna array consists of a C-shaped monopole on the upper layer functioning as the radiating patch; and an octagonal-ring slot patch on the lower layer functioning as the ground plane. The four elements are connected by a sequentially-rotated feed network to enhance the impedance bandwidth (IBW), axial ratio bandwidth (ARBW), and gain. Simulations are performed, and an antenna prototype is fabricated and experiments carried out. The measured IBW and ARBW at the center frequency of 2.4 GHz are 91.6% (1.8 – 4 GHz) and 84.5% (1.97 – 4 GHz), with the maximum gain of 7.8 dBic at 3.3 GHz, rendering the proposed four-element CP octagonal-ring slot antenna array with sequentially-rotated feed network operationally suitable for S-band satellite communication. The novelty of this research lies in the use of CMA to characterize the circular polarization of the octagonal-ring slot antenna array; and the sequentially-rotated feed network to enhance the IBW, ARBW, and antenna gain of the four-element CP octagonal-ring slot antenna array with sequentially-rotated feed network.

INDEX TERMS Antenna arrays, characteristic mode analysis, impedance, satellite communication, slot antennas.

I. INTRODUCTION

In recent decades, small satellites have been increasingly adopted by the space industry [1]. The purposes of small satellites include research and science, remote sensing, communications, weather forecast, Internet of Things, and exploration [2], [3]. The advantages of small satellites are light weight, low cost, compactness and ease of manufacturing. Small satellites can be classified by weight as minisatellite (100 – 500 kg), microsatellite (10 – 100 kg), nanosatellite (1 – 10 kg), picosatellite (0.1 – 1 kg), and femtosatellite (less than 0.1 kg) [4], [5].

Cube satellites (CubeSat) are a type of low Earth orbit (LEO) nanosatellite [6]. There are five types of CubeSats: 1U (10 cm × 10 cm × 10 cm), 2U (10 cm × 10 cm × 20 cm), 3U (10 cm × 10 cm × 30 cm), 6U (10 cm × 20 cm × 30 cm), and 12U (10 cm × 10 cm × 60 cm) [7]. CubeSats are typically adopted in the telemetry, tracking and commanding (TTC) subsystem [8]. As a result, CubeSats require reliable and efficient antennas to transmit and receive the downlink and

The associate editor coordinating the review of this manuscript and approving it for publication was Sotirios Goudos.

uplink signals between the ground station and the satellite. Depending on the missions, the CubeSat antennas can be of VHF (30 – 300 MHz), UHF (0.3 – 3 GHz), L (1 – 2 GHz), S (2 – 4 GHz), C (4 – 8 GHz), X (8 – 12 GHz), Ku (12 – 18 GHz), and Ka (26.5 – 40 GHz) bands.

The vital characteristic of the CubeSat antennas is circular polarization to minimize the fading and multipath interference in space [9]. The circularly polarized (CP) antennas come in many shapes and forms, including dipole, monopole, patch, patch array, slot, metasurface (MTS), reflector, helical, horn, and reflectarray [10], [11]. Of particular interest is the CP planar antenna (e.g., patch, patch array, slot, and metasurface) [12], [13] because of its straightforwardness, compactness, low cost, and ease of installation. Nevertheless, the planar CP antenna for the CubeSat requires wide impedance bandwidth (IBW) and axial ratio bandwidth (ARBW).

In [14] and [15], characteristic mode analysis (CMA) was used to characterize the CP planar antennas. The CMA is an analysis methodology to characterize the surface current and radiating field of the CP planar antenna using the modal resonance [16]. Specifically, in [17], a clock-shaped bidirectional CP antenna using CMA for S-band spectrum achieves an IBW and 3-dB ARBW of 84.6% (2.38 – 5.8 GHz) and 43.4% (2.4 – 3.73 GHz). In [18], a single-fed U-slot CP patch antenna using CMA for C-band spectrum achieves an IBW of 29% (4.7 – 6.3 GHz), 3-dB ARBW of 20.9% (4.95 – 6.1 GHz), and maximum gain of 7.3 dBic at 5.2 GHz. In [19], a CMA-based single-fed CP loop antenna with two inductors for S-band spectrum achieves an IBW of 58.3% (2.2 – 3.6 GHz), 3-dB ARBW of 7.5% (2.32 – 2.5 GHz), and maximum gain of 6.52 dBic at 2.4 GHz. In [20], a CMA-based bidirectional CP grid-slot patch antenna with double-layer of 4 × 4 square-patch metasurface (MTS) and Z-shaped slot ground plane for C-band spectrum achieves an IBW of 38.3% (4.05 – 5.97 GHz), 3-dB ARBW of 21% (4.08 – 5 GHz), and maximum gain of 3.5 dBic at 4.7 GHz.

In [21], a CP patch antenna using CMA with 4 × 4 H-shaped MTS for C-band spectrum achieves an IBW of 38.8% (4.42 – 6.55 GHz), 3-dB ARBW of 14.3% (5.2 – 6 GHz), and maximum gain of 9.4 dBic at 5 GHz. In [22], a CMA-based non-uniform MTS antenna using strip-line feed line for S-band spectrum achieves an IBW of 17.7% (1.95 – 2.34 GHz), 3-dB ARBW of 13.6% (2.09 – 2.39 GHz), and maximum gain of 8 dBic at 2.2 GHz. In [23], a CMA-based square-shaped MTS CP patch antenna with cross-slot ground plane and sequentially-rotated feed network for C-band spectrum achieves an IBW of 28.2% (4.8 – 6.35 GHz), 3-dB ARBW of 20.9% (4.85 – 6 GHz), and maximum gain of 9.5 dBic at 5.9 GHz.

In [24], a CP slot monopole antenna using CMA consisting of a C-shaped monopole and C-shaped slot ground plane for S- and C-band spectra achieves an IBW of 91% (2.1 – 5.6 GHz), 3-dB ARBW of 91% (2.1 – 5.6 GHz), and maximum gain of 3.2 dBic at 3 GHz. In [25], a CMA-based CP hexagon-shaped antenna for S- and C-band spectra achieves an IBW of 107% (2.3 – 7.6 GHz), 3-dB ARBW of 59.9% (3.45 – 6.4 GHz), and maximum gain of 4.6 dBic at 4.8 GHz. In [26], the authors comparatively investigated two CMA-based CP antenna schemes for S-band spectrum, consisting of U-slot and E-shaped patch antennas; and reported that the U-slot patch antenna achieved an IBW of 11.81% (2.24 – 2.5 GHz) and 3-dB ARBW of 4.54% (2.27 – 2.37 GHz), while the E-shaped patch antenna achieved an IBW of 9.54% (2.35 – 2.56 GHz) and 3-dB ARBW of 15.9% (2.2 – 2.55 GHz).

Specifically, this research proposes a low-complexity and low-profile four-element CP octagonal-ring slot antenna array with sequentially-rotated feed network for S-band satellite applications. In the study, the proposed antenna array is characterized by CMA. One single element of the CP octagonal-ring slot antenna array consists of a C-shaped monopole on the upper layer functioning as the radiating patch; and an octagonal-ring slot patch on the lower layer functioning as the ground plane. The four elements are connected by a sequentially-rotated feed network to enhance the IBW, ARBW, and gain. Simulations are performed, and an antenna prototype is fabricated and experiments carried out.

The organization of this research is as follows: Section I is the introduction. Section II is concerned with the characteristic mode analysis to characterize the circular polarization of a planar antenna. Section III details the antenna design, specifically one single element of the proposed CP octagonal-ring slot antenna array by using CMA. Section IV describes the proposed four-element CP octagonal-ring slot antenna array with sequentially-rotated feed network, and Section V discusses the experimental results. The conclusions are provided in Section VI.

II. CMA-BASED CP PLANAR ANTENNA

In [27], the theory of characteristic modes was proposed to characterize the surface current and radiating field on perfect electrical conductor (PEC) bodies. The characteristics of the surface current and radiating field are determined by the configuration and dimension of the conducting structure. In [28], characteristic mode analysis (CMA) was utilized in the planner antenna design. The characteristic mode (CM; J) is calculated by equation (1) [29].

$$J = \sum_{n} C_n J_n \tag{1}$$

where J_n is the characteristic current of n^{th} mode and C_n is the complex modal weighting coefficient (MWC). The MWC can be calculated by equation (2) [30].

$$C_n = \frac{V_n^i}{1 + j\lambda_n} \tag{2}$$

where λ_n is an eigenvalue and V_n^i is the modal excitation coefficient (MEC). The CM current ($|C_n|$) can be calculated by equation (3) [31].

$$|C_n| = \left| \frac{V_n^i}{1 + j\lambda_n} \right| = \left| V_n^i \right| MS \tag{3}$$

where MS is the modal significance which is the normalized amplitude of the CM current, as expressed in equation (4) [32], given that MS must be greater than or equal to 0.707 [33].

$$MS_n = \frac{1}{1 + j\lambda_n} \tag{4}$$

The characteristic angle (CA) is the phase difference between the characteristic current (J_n) and the corresponding characteristic field, which can be calculated by equation (5) [34].

$$CA_n = 180^\circ - \tan^{-1}(\lambda_n) \tag{5}$$

To realize CP radiation, the modal current distributions between two modes must be orthogonal. Besides, the MS between two orthogonal modes are identical and the phase difference of their characteristic angles is approximately $\pm 90^\circ$.

III. DESIGN OF CP OCTAGONAL-RING SLOT ANTENNA

In the design of the antenna, the characteristic mode analysis was carried out using CST Microwave Studio Suite (Multilayer Solver). In this research, the CMA is utilized to characterize the surface current and radiating field of the PEC (i.e., C-shaped monopole) and lossless dielectric material (i.e., FR-4 substrate). The evolution of the C-shaped monopole consists of three stages: circular ring patch, C-shaped patch, and octagonal-ring slot antenna with C-shaped monopole feed network.

A. CIRCULAR RING PATCH

Figure 1(a) shows the geometry of the circular ring patch without feed network and ground plane, and Figure 1(b) illustrates the radiation boundary of the circular ring patch without feed network and ground plane. The circular ring patch is excited in the x-, y-, and z-directions. The circular ring patch is a PEC material sitting on the upper layer of a lossless FR-4 substrate. The dielectric constant (ε_r) and thickness of the FR-4 substrate are 4.3 and 1.6 mm, with 60 mm × 60 mm in dimension. The inner (R_{ri}) and outer radii (R_{ro}) of the circular ring patch are 4 mm and 17.5 mm.

Figures 2(a)-(b) show the simulated CMA results of the circular ring patch. In Figure 2(a), the MS of Mode 1 (J_1) and Mode 2 (J_2) are identical and greater than 0.707 between 3 GHz – 4 GHz. Meanwhile, the MS of Mode 3 (J_3) and Mode 4 (J_4) are lower than 0.707. In Figure 2(b), the phase difference of the CA between Modes 1 and 2 is 0°, while that between Modes 3 and 4 is excessively larger than 90°. Figures 3(a)-(b) show, as an example, the current distribution on the circular ring patch of Mode 1 (J_1) and Mode 2 (J_2) at 3.2 GHz, which is orthogonal.

Figure 4(a) shows the geometry of the C-shaped patch without feed network and ground plane. Figure 4(b) shows the radiation boundary of the C-shaped patch without feed network and ground plane. The C-shaped patch is excited in the x-, y-, and z-directions. To realize circular polarization, the circular ring patch (Figure 1) is truncated by θ° such that

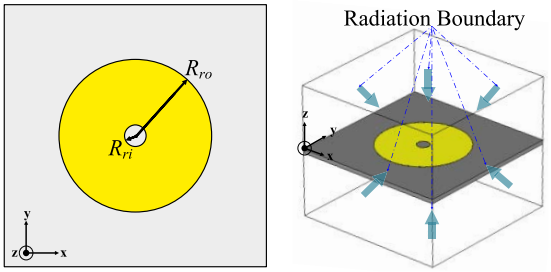

FIGURE 1. The circular ring patch: (a) geometry, (b) radiation boundary.

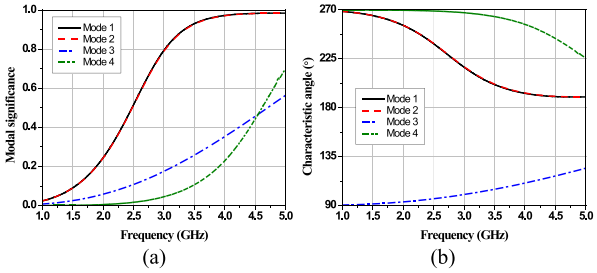

FIGURE 2. Simulated results of CMA of the circular ring patch: (a) MS, (b) CA.

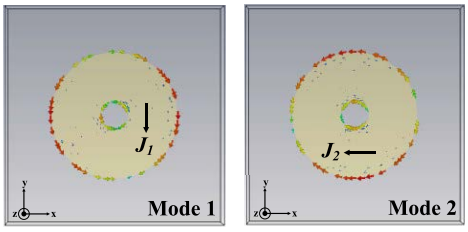

FIGURE 3. Current distribution at 3.2 GHz of the circular ring patch: (a) Mode 1, (b) Mode 2.

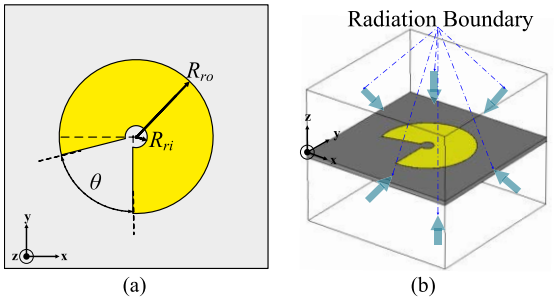

FIGURE 4. The C-shaped patch: (a) geometry, (b) radiation boundary.

the phase difference of the CA between Mode 1 and Mode 2 is orthogonal.

Figures 5(a)-(b) show the simulated MS and CA of the C-shaped patch. The MS of Mode 1 and Mode 2 of the C-shaped patch at 3.2 GHz, as an example, are identical (0.72), with 94° phase difference. Figures 6(a)-(b) show the corresponding surface current distribution at 3.2 GHz of

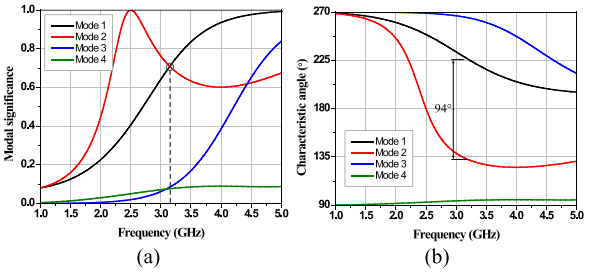

FIGURE 5. Simulated results of CMA of the C-shaped patch: (a) MS, (b) CA.

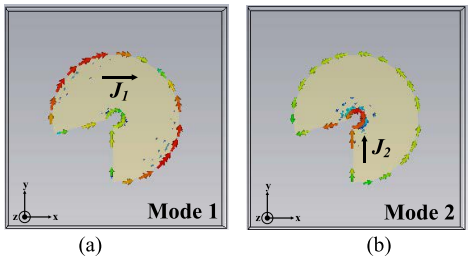

FIGURE 6. Current distribution of the C-shaped patch at 3.2 GHz: (a) Mode 1, (b) Mode 2.

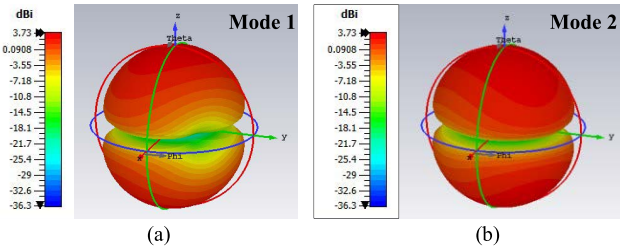

FIGURE 7. Far-field radiation pattern of the C-shaped patch at 3.2 GHz: (a) Mode 1, (b) Mode 2.

Mode 1 (J_1) and Mode 2 (J_2). The surface current of Mode 1 (J_1) and Mode 2 (J_2) orthogonally travel along the inner and outer edge of the C-shaped patch. Figures 7(a)-(b) show the corresponding 3D far-field radiation patterns at 3.2 GHz of Mode 1 and Mode 2 of the C-shaped patch. The far-field radiation pattern of Mode 1 and Mode 2 which is of CP radiation.

B. RECTANGULAR-RING SLOT PATCH

Figure 8(a) shows geometry of the rectangular-ring slot patch without corners truncation. The rectangular-ring slot patch functions as the ground plane. Figure 8(b) shows the radiation boundary of the rectangular-ring slot patch without feed network. The rectangular-slot patch is excited in the x-, y-, and z-directions.

Figures 9(a)-(b) show simulated MS and CA of the rectangular-ring slot patch. The MS of Mode 1 and Mode 2 of 0.77 are identical at 2.2 GHz, with 79° phase difference, and the MS of Mode 1 and Mode 5 of 0.84 are identical at 3.31 GHz, with 70° phase difference. Meanwhile, the MS of

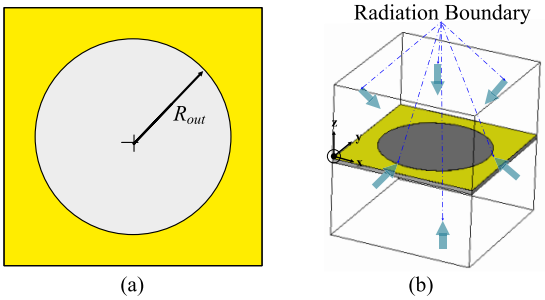

FIGURE 8. The rectangular-ring slot patch: (a) geometry, (b) radiation boundary.

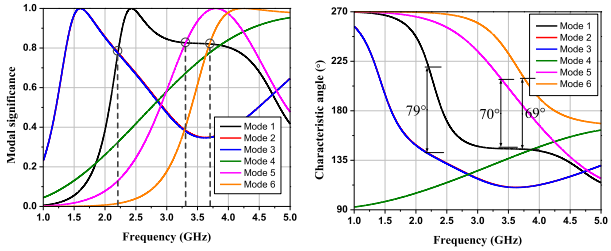

FIGURE 9. Simulated results of CMA of the rectangular-ring slot patch: (a) MS, (b) CA.

Mode 1 and Mode 6 (0.82) are identical at 3.7 GHz, with 69° phase difference.

Figures 10(a)-(c) illustrate the current distribution of the rectangular-ring slot patch at 2.2, 3.31, and 3.7 GHz, respectively. In Figure 10(a), the surface current of Mode 1 (J_1) and Mode 2 (J_2) travel orthogonally along the edge of the circular slot of the rectangular patch. In Figure 10(b), the surface current of Mode 1 (J_1) and Mode 5 (J_5) travel in the opposite direction along the inner of the circular slot and along the edge of the rectangular patch. In Figure 10(c), the surface current of Mode 1 (J_1) and Mode 6 (J_6) travel in the opposite direction along the edge of the circular slot and along the edge of the rectangular patch.

Figures 11(a)-(c) show the 3D far-field radiation patterns of the rectangular-ring slot patch at 2.2, 3.31, and 3.7 GHz, respectively. The far-field radiation patterns of Modes 1&2 and Modes 1&5 are of symmetric-lobe radiation. Meanwhile, the radiation patterns of Modes 1&6 are of non-CP radiation. Especially, the surface current of Modes 1 and 2 of the rectangular-ring slot patch at 2.2 GHz are orthogonal, resulting in the CP radiation.

C. OCTAGONAL-RING SLOT PATCH

Figure 12(a) shows the geometry of the octagonal-ring slot patch without feed network. The octagonal-ring slot patch is of circular slot with truncated corners, functioning as the ground plane. Figure 12(b) shows the radiation boundary of the octagonal-ring slot patch without feed network. The octagonal-ring slot is excited in the x-, y-, and z-directions. Figure 13(a)-(b) show simulated MS and CA of

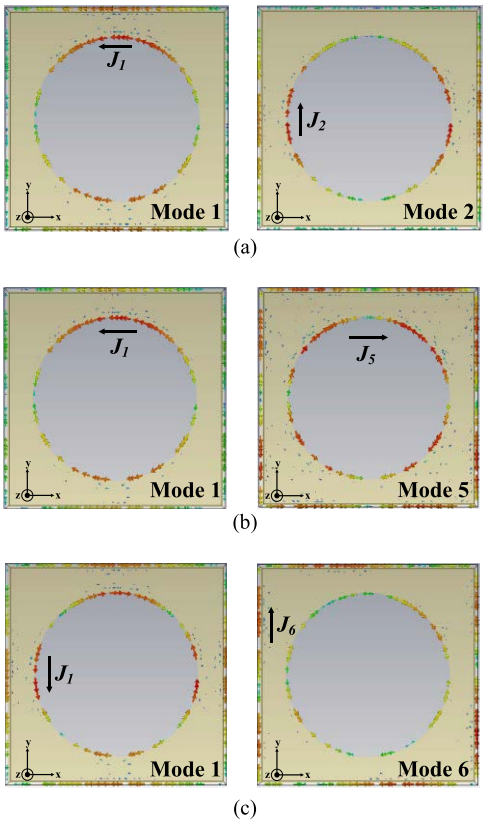

FIGURE 10. Current distribution of the rectangular-ring slot patch at: (a) 2.2 GHz, (b) 3.31 GHz, (c) 3.7 GHz.

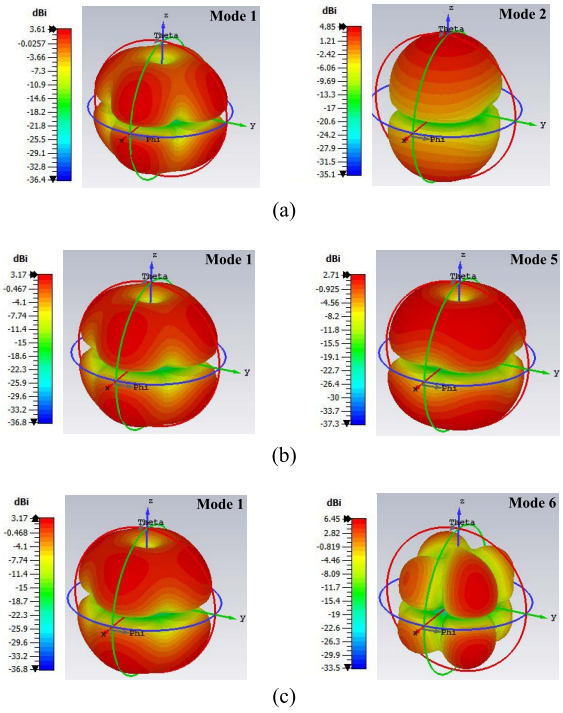

FIGURE 11. Far-field radiation patterns of the rectangular-ring slot patch at: (a) 2.2 GHz, (b) 3.31 GHz, (c) 3.7 GHz.

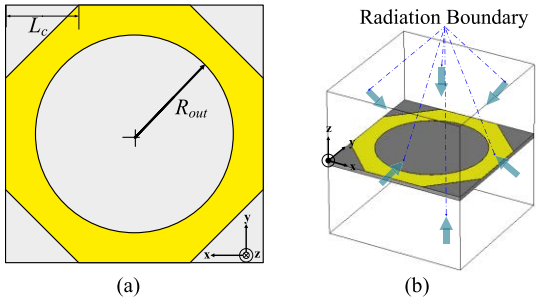

FIGURE 12. The octagonal-ring slot patch: (a) geometry, (b) radiation boundary.

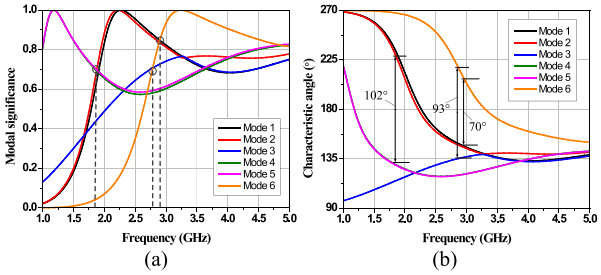

FIGURE 13. Simulated results of CMA of the octagonal-ring slot patch: (a) MS, (b) CA.

the octagonal-ring slot patch. The MS of Mode 2 and Mode 5 of 0.71 are identical at 1.83 GHz, with 102° phase difference, and the MS of Mode 3 and Mode 6 of 0.72 are identical at 2.77 GHz, with 93° phase difference. Meanwhile, the MS of Mode 1 and Mode 6 (0.84) are identical at 2.9 GHz, with 70° phase difference.

Figures 14(a)-(c) illustrate the current distribution of the octagonal-ring slot patch at 1.83, 2.77, and 2.9 GHz, respectively. In Figure 14(a), the surface current of Mode 2 (J_2) and Mode 5 (J_5) travel orthogonally along the inner edge of the circular slot and the outer edge of the octagonal patch. In Figure 14(b), the orthogonal surface current of Mode 3 (J_3) and Mode 6 (J_6) travel along the inner edge of the circular slot. In Figure 14(c), the surface current of Mode 1 (J_1) and Mode 6 (J_6) travel orthogonally along the inner edge of the circular slot and the outer edge of the octagonal patch.

Figures 15(a)-(c) show the 3D far-field radiation patterns of the octagonal-ring slot patch at 1.83, 2.77, and 2.9 GHz, respectively. The far-field radiation patterns of Modes 2&5, Modes 3&6, and Modes 1&6 are of symmetric-lobe radiation (i.e., CP radiation).

D. THE CP OCTAGONAL-RING SLOT ANTENNA WITH C-SHAPED MONOPOLE

Figures 16(a)-(c) depict the front, rear and perspective views of the CP octagonal-ring slot antenna with C-shaped monopole. The CP octagonal-ring slot antenna with C-shaped monopole is realized by using FR-4 substrate with 1.6 mm in thickness and 60 mm × 60 mm ($W_s \times W_s$) in dimension.

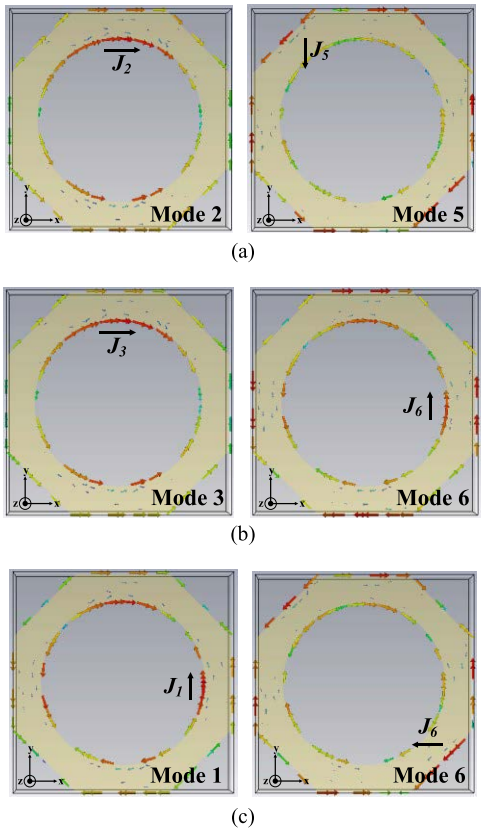

FIGURE 14. Current distribution of the octagonal-ring slot patch at: (a) 1.83 GHz, (b) 2.77 GHz, (c) 2.9 GHz.

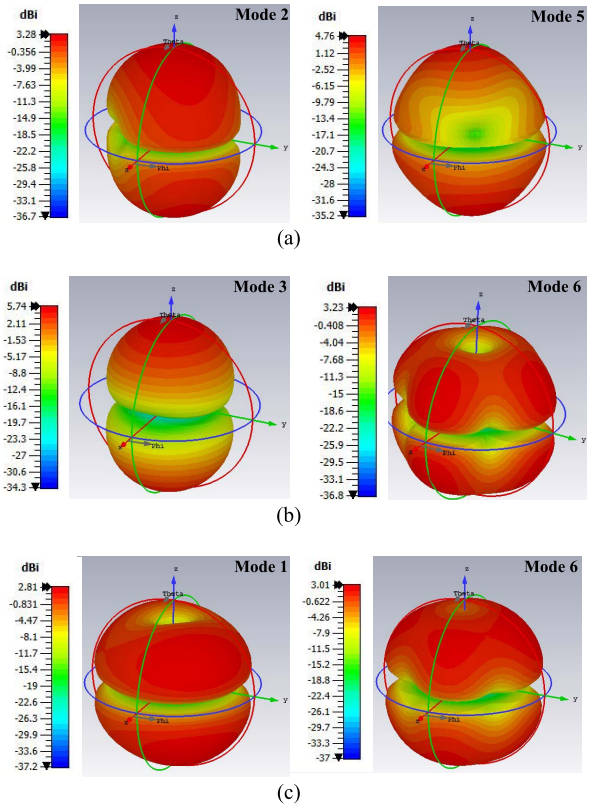

FIGURE 15. Far-field radiation pattern of the octagonal-ring slot patch at: (a) 1.83 GHz, (b) 2.77 GHz, (c) 2.9 GHz.

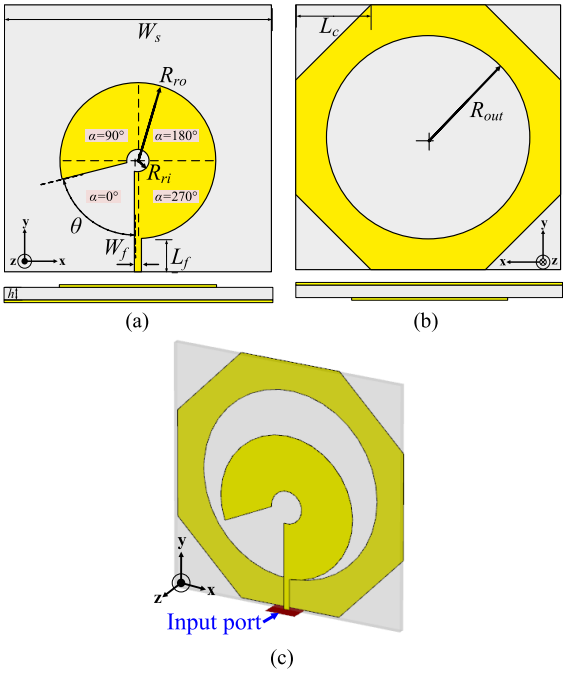

FIGURE 16. Geometry of the CP octagonal-ring slot antenna with C-shaped monopole: (a) front view, (b) rear view, (c) perspective view.

The upper layer of the substrate consists of the C-shaped monopole functioning as the radiating patch [35], with the circular patch radius (R_{ro}) of 17.5 mm, the circular slot radius (R_{ri}) of 4 mm, and the microstrip feed line dimension ($W_f \times L_f$) of 1.5 mm × 7.5 mm. Meanwhile, on the lower layer of the substrate sits the octagonal-ring slot functioning as the ground plane, with the circular slot radius (R_{out}) of 24 mm, the corner-truncated length (L_c) of 17 mm, the arc truncation (θ) of 30°, and the arc truncated position (α) of 0°.

Figures 17(a)-(b) show the simulated impedance bandwidth (IBW) and axial ratio bandwidth (ARBW) of the CP octagonal-ring slot antenna with C-shaped monopole, respectively. In Figure 17(a), the simulated IBW ($|S_{11}| \leq -10$ dB) at the center frequency of 2.4 GHz is 95% (1.72 – 4 GHz), covering the entire S-band spectrum (2 – 4 GHz). In Figure 17(b), the simulated ARBW (AR $\leq$ 3 dB) occurs between 2 – 2.4 GHz and 3 – 3.5 GHz, failing to cover the entire S-band spectrum.

To achieve wideband circular polarization that covers the entire S-band spectrum, the key parameters of the CP octagonal-ring slot antenna with C-shaped monopole are further optimized. The key parameters include the circular slot radius (R_{out}), the corner-truncated length (L_c), the arc truncation (θ), the arc truncated position (α), and the inner radius of the circular ring patch (R_{ri}).

Figures 18(a)-(b) show the simulated IBW and ARBW under different circular slot radius (R_{out}): 22, 23, and 24 mm. In Figure 18(a), the IBW shifts to higher frequency as R_{out} increases. With $R_{out} = 22$ and 24 mm, an impedance mismatch ($|S_{11}| > -10$ dB) occurs between 2.8 – 2.9 GHz

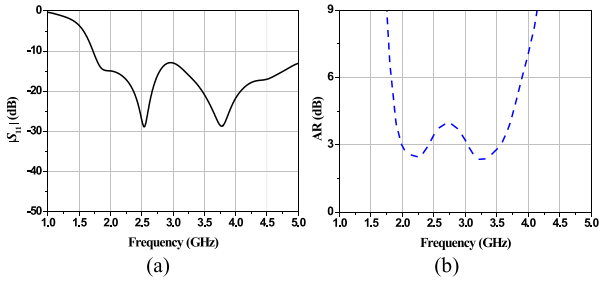

FIGURE 17. Simulated results of the CP octagonal-ring slot antenna with C-shaped monopole: (a) IBW, (b) ARBW.

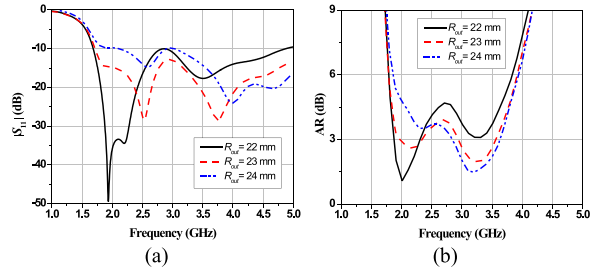

FIGURE 18. Simulated results of the CP octagonal-ring slot antenna with C-shaped monopole under variable R_{out}: (a) IBW, (b) ARBW.

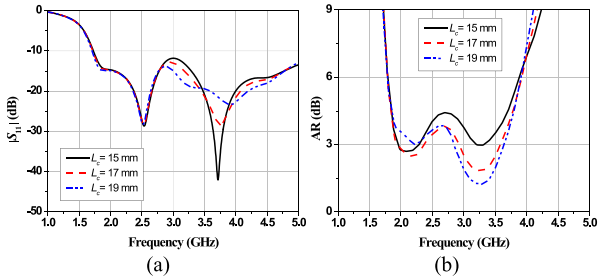

FIGURE 19. Simulated results of the CP octagonal-ring slot antenna with C-shaped monopole under variable L_c: (a) IBW, (b) ARBW.

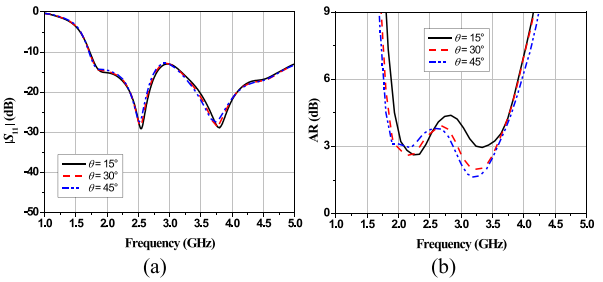

FIGURE 20. Simulated results of the CP octagonal-ring slot antenna with C-shaped monopole under variable θ: (a) IBW, (b) ARBW.

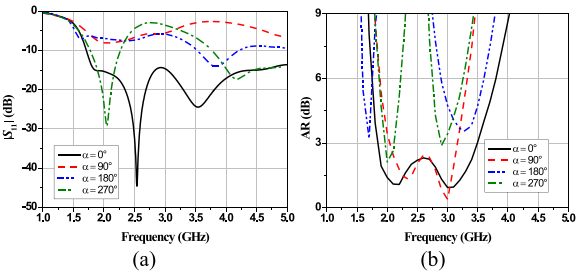

FIGURE 21. Simulated results of the CP octagonal-ring slot antenna with C-shaped monopole under variable α: (a) IBW, (b) ARBW.

and 2.9 – 3 GHz, respectively. With $R_{out} = 23$ mm, the IBW falls between 1.73 – 4 GHz, covering the entire S-band spectrum (2 – 4 GHz). In Figure 18(b), with $R_{out} = 22$ mm, ARBW (AR $\leq$ 3 dB) is narrow, covering 1.85 – 2.34 GHz. With $R_{out} = 23$ mm, ARBW is between 1.95 – 2.34 GHz and 2.94 – 3.56 GHz. With 24 mm, ARBW falls between 2.83 – 3.63 GHz. As a result, the chosen R_{out} is 23 mm.

Figures 19(a)-(b) show the simulated IBW and ARBW under different corner-truncated length of the octagonal-ring slot (L_c): 15, 17, and 19 mm. In Figure 19(a), variation in L_c has minimal effect on $|S_{11}|$ of the first resonance at 2.5 GHz, while $|S_{11}|$ of the second resonance at 3.71 GHz increases as L_c increases. In Figure 19(b), with $L_c = 15$ mm, ARBW (AR $\leq$ 3 dB) is between 1.96 – 2.3 GHz. With $L_c = 17$ mm, ARBW occurs between 1.97 – 2.34 GHz and 2.94 – 3.56 GHz. The ARBW falls between 2.84 – 3.64 GHz for $L_c = 19$ mm. The chosen L_c is 17 mm.

Figures 20(a)-(b) show the simulated IBW and ARBW under different arc truncation of the C-shaped monopole (θ): 15°, 30°, and 45°. In Figure 20(a), as θ increases, $|S_{11}|$ of the first and second resonance slightly deteriorate (from −29 dB to −26 dB and −28 dB to −26 dB, respectively). In Figure 20 (b), with $\theta = 15°$, ARBW (AR $\leq$ 3 dB) is between 2.12 – 2.45 GHz. Meanwhile, ARBW occurs between 1.97 – 2.35 GHz and 2.93 – 3.56 GHz for $\theta = 30°$. With $\theta = 45°$, ARBW falls between 2.87 – 3.57 GHz. The chosen θ is 30°.

Figures 21(a)-(b) show the simulated IBW and ARBW under different arc-truncation position of the C-shaped monopole (α): 0°, 90°, 180°, and 270°. In Figure 21(a), with $\alpha = 90°$, an impedance mismatch occurs ($|S_{11}| > -10$ dB). With $\alpha = 180°$, the IBW falls between 3.5 – 4.2 GHz. With $\alpha = 270°$, $|S_{11}|$ of the first and second resonance fall between 1.77 – 2.27 GHz and 3.77 – 4 GHz, respectively. With $\alpha = 0°$, IBW falls between 1.71 – 4 GHz. In Figure 21(b), with $\alpha = 180°$ and 270°, the ARBW (ARBW > 3dB) fails to cover the S-band spectrum. With $\alpha = 0°$ and 90°, ARBW falls between 1.84 – 3.5 GHz and 2.05 – 3.16 GHz, respectively. As a result, the chosen α is 0°.

Figures 22(a)-(b) show the simulated IBW and ARBW under different radii of the circular slot of the C-shaped monopole (R_{ri}): 3, 4, and 5 mm. In Figure 22(a), as R_{ri} increases, $|S_{11}|$ of the first resonance improves (from −26.4 dB to −40 dB), while the second resonance slightly shifts to higher frequency. In Figure 22(b), with $R_{ri} = 3$ mm, ARBW (AR $\leq$ 3 dB) occurs between 2 – 2.5 GHz and 2.95 – 3.62 GHz. With $R_{ri} = 4$ and 5 mm, ARBW are between 1.84 – 3.5 GHz and 1.8 – 3.2 GHz, respectively. The chose R_{ri} is 4 mm. Table 1 tabulates the parameters and dimensions of the single element of the CP octagonal-ring slot antenna array.

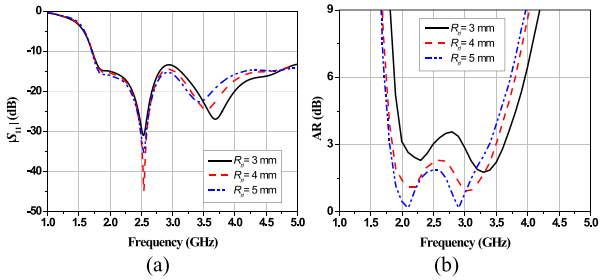

FIGURE 22. Simulated results of the CP octagonal-ring slot antenna with C-shaped monopole under variable R_{ri}: (a) IBW, (b) ARBW.

TABLE 1. Parameters and dimensions of the single element of the CP octagonal-ring slot antenna array.

Parameters	W_s	R_{ro}	R_{ri}	W_f	L_f	θ	α	L_c	R_{out}
Values (mm)	60	17.5	4	1.5	7.5	30°	0°	17	23

Figures 23(a)-(b) show the simulated MS and phase difference of CA of the single element of the CP octagonal-ring slot antenna array. One single element consists of the CP octagonal-ring slot antenna and the C-shaped monopole, given the optimal parameters (Table 1). The MS of Mode 1 and Mode 6 at 1.8 GHz are identical (0.77), with 80° phase difference, and those of Mode 1 and Mode 2 at 2.74 GHz are also identical (0.82), with 70° phase difference. The MS of Mode 1 and Mode 4 at 2.8 GHz are identical (0.77), with 80° phase difference, while those of Mode 1 and Mode 5 at 2.85 GHz are identical (0.72), with 87° phase difference. Besides, the MS of Mode 2 and Mode 5 at 3.35 GHz are also identical (0.91), with 50° phase difference. Essentially, the CMA could be deployed to characterize and verify the circular polarization of the single element of the CP octagonal-ring slot antenna array. The CMA results are consistent with the results of the full-wave simulation (Figure 24).

Figures 24(a)-(b) show the simulated IBW and ARBW of the single element of the CP octagonal-ring slot antenna array. The simulated IBW and ARBW are 95.4% (1.71 – 4 GHz) and 69% (1.84 – 3.5 GHz) at the center frequency of 2.4 GHz. Despite the wide IBW and ARBW, the ARBW (AR $\leq$ 3 dB) fails to cover the entire S-band spectrum (2 – 4 GHz). As a result, of the single element of the CP octagonal-ring slot antenna array is augmented with sequentially-rotated feed network to improve the ARBW.

E. DIFFERENT SHAPES OF THE SLOT PATCH GROUND PLANE AND THE MONOPOLE

Figures 25(a)-(b) show the simulated IBW and ARBW of the rectangular-ring slot ground plane under different monopole shapes (i.e., rectangular, pentagonal, hexagonal, octagonal, and circular). In Figure 25(a), $|S_{11}|$ of the rectangular monopole fails to cover the S-band spectrum (2 – 4 GHz). $|S_{11}|$ of the first and second resonance of the octagonal monopole fall between 1.6 – 2.52 GHz and

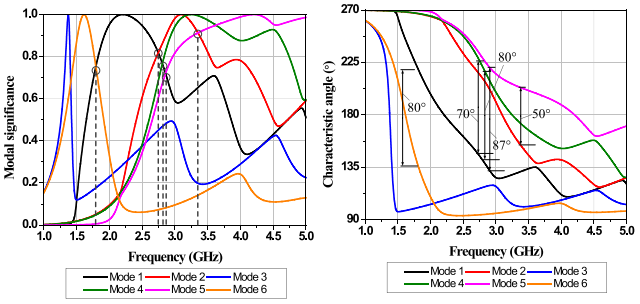

FIGURE 23. Simulated CMA of the proposed single element of the CP octagonal-ring slot antenna array: (a) MS, (b) CA.

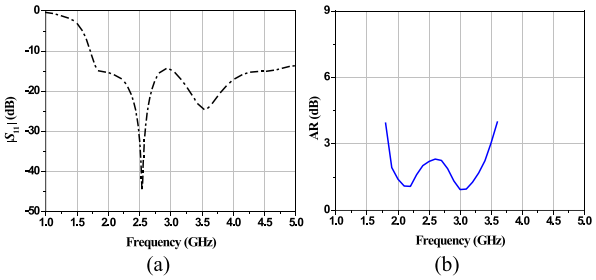

FIGURE 24. Simulated results of one single element of the CP octagonal-ring slot antenna array: (a) IBW, (b) ARBW.

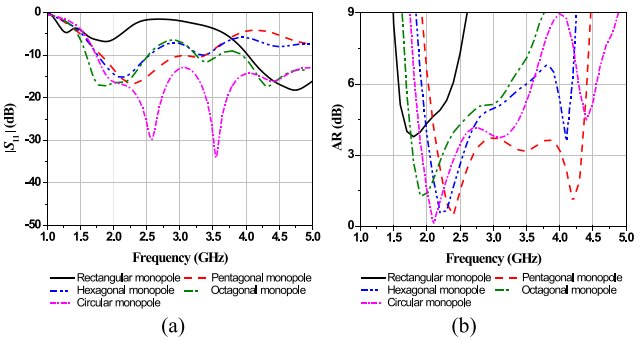

FIGURE 25. Simulated results of the rectangular-ring slot ground plane under different monopole shapes: (a) IBW, (b) ARBW.

3.23 – 3.61 GHz. Besides, the IBW of the pentagonal, hexagonal, and circular monopoles are between 1.78 – 3.4 GHz, 1.76 – 2.53 GHz, and 1.74 – 4 GHz. In Figure 25(b), the ARBW of the rectangular monopole is greater than 3 dB. The ARBW of the pentagonal, hexagonal, octagonal, and circular monopoles are between 2 – 2.54 GHz, 2.1 – 2.4, 1.78 – 2.22 GHz, and 1.91 – 2.44 GHz, respectively.

Figures 26(a)-(b) show the simulated IBW and ARBW of the pentagonal-ring slot ground plane under different monopole shapes. In Figure 26(a), $|S_{11}|$ of the rectangular monopole fails to cover the S-band spectrum. $|S_{11}|$ of the pentagonal and hexagonal monopole are between 1.71 – 3 GHz and 1.71 – 2.5 GHz. $|S_{11}|$ of the first and second resonance of the octagonal monopole fall between 1.6 – 2.52 GHz and 3.23 – 3.61 GHz. The IBW of the circular monopoles is

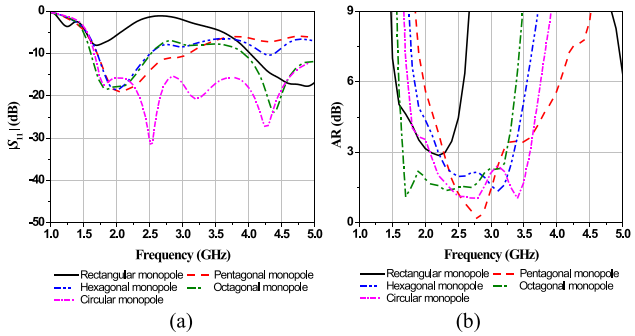

FIGURE 26. Simulated results of the pentagonal-ring slot ground plane under different monopole shapes: (a) IBW, (b) ARBW.

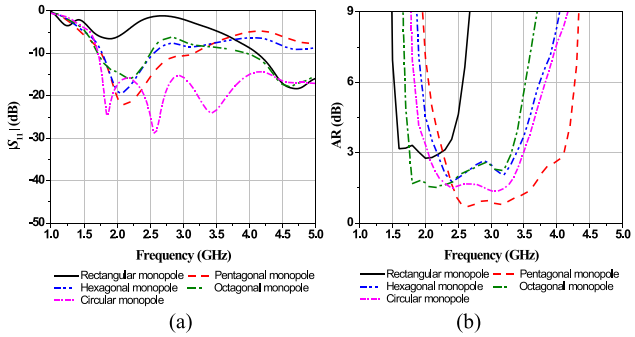

FIGURE 27. Simulated results of the hexagonal-ring slot ground plane under different monopole shapes: (a) IBW, (b) ARBW.

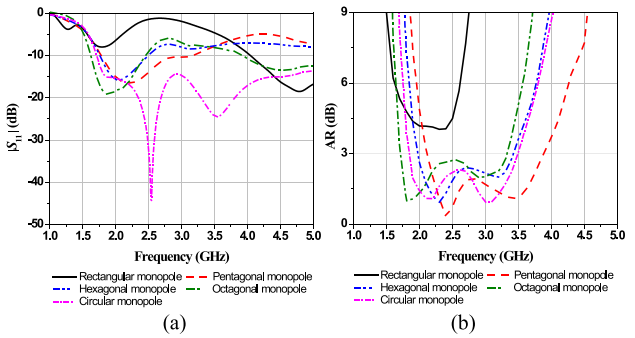

FIGURE 28. Simulated results of the octagonal-ring slot ground plane under different monopole shapes: (a) IBW, (b) ARBW.

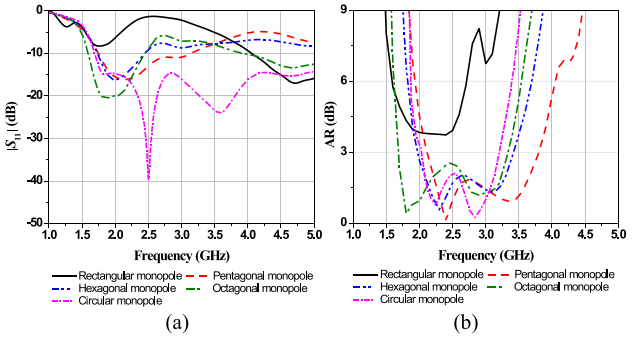

FIGURE 29. Simulated results of the circular-ring slot ground plane under different monopole shapes: (a) IBW, (b) ARBW.

1.66 – 4 GHz. In Figure 26(b), the ARBW of the rectangular, pentagonal, hexagonal, octagonal, and circular monopoles are between 2.1 – 2.3 GHz, 2.27 – 2.4, 2.24 – 3.34 GHz, and 2 – 3.59 GHz, respectively.

Figures 27(a)-(b) show the simulated IBW and ARBW of the hexagonal-ring slot ground plane under different monopole shapes. In Figure 27(a), $|S_{11}|$ of the rectangular monopole fails to cover the S-band spectrum. $|S_{11}|$ of the pentagonal, hexagonal, octagonal, and circular monopoles are between 1.76 – 3.15 GHz, 1.78 – 2.55 GHz, 1.71 – 2.52 GHz, and 1.72 – 4 GHz. In Figure 27(b), the ARBW of the rectangular, pentagonal, hexagonal, octagonal, and circular monopoles are between 2.29 – 4 GHz, 2.27 – 2.4, 2.2 – 3.37 GHz, 1.77 – 3.3 GHz, and 2 – 3.46 GHz.

Figures 28(a)-(b) show the simulated IBW and ARBW of the octagonal-ring slot ground plane under different monopole shapes. In Figure 28(a), $|S_{11}|$ of the rectangular monopole fails to cover the S-band spectrum. $|S_{11}|$ of the pentagonal, hexagonal, octagonal, and circular monopoles are between 1.79 – 3.16 GHz, 1.75 – 2.51 GHz, 1.62 – 2.48 GHz, and 1.71 – 4 GHz. In Figure 28(b), the ARBW of the rectangular monopole is greater than 3 dB. The ARBW of the pentagonal, hexagonal, octagonal, and circular monopoles are between 2.12 – 3.88 GHz, 3 – 3.42, 1.72 – 3.31 GHz, and 1.84 – 3.5 GHz.

Figures 29(a)-(b) show the simulated IBW and ARBW of the circular-ring slot ground plane under different monopole shapes. The $|S_{11}|$ of the pentagonal, hexagonal, octagonal, and circular monopoles are between 1.75 – 3.14 GHz, 1.74 – 2.44 GHz, 1.6 – 2.46 GHz, and 1.68 – 4 GHz. In Figure 29(b), the ARBW of the rectangular monopole is greater than 3 dB. The ARBW ($\leq$ 3dB) of the pentagonal, hexagonal, octagonal, and circular monopoles are between 2.1 – 3.79 GHz, 2 – 3.4, 1.68 – 3.33 GHz, and 2.1 – 3.24 GHz.

IV. THE CP OCTAGONAL-RING SLOT ANTENNA ARRAY WITH SEQUENTIALLY-ROTATED FEED NETWORK

Figures 30(a)-(b) respectively illustrate the front and rear of the CMA-based CP octagonal-ring slot antenna array with sequentially-rotated feed network for S-band satellite applications. The proposed CMA-based CP octagonal-ring slot antenna array sits on an FR-4 substrate of 120 mm $\times$ 120 mm ($W_{sub} \times W_{sub}$) in dimension and 1.6 mm in thickness (h).

The upper layer of the substrate contains 2 $\times$ 2 C-shaped monopoles connected by a sequentially-rotated feed network, and the lower layer of the substrate consists of four elements of the octagonal-ring slot ground plane. The four elements are arranged corresponding to the sequentially-rotated feed network fed by an SMA connector. The sequentially-rotated feed network is a transmission line model which uses a quarter-wavelength transformer technique to achieve impedance matching [36]. Thus, the sequentially-rotated feed network provides the phase quadrature with equal magnitude for each output port. Table 2 tabulates the parameters and optimal

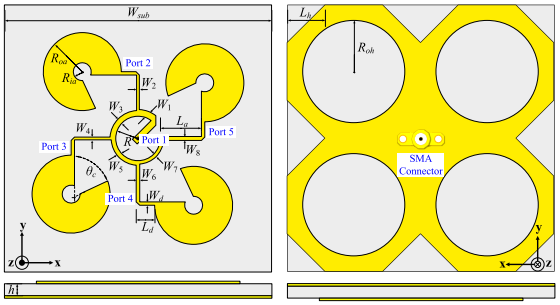

FIGURE 30. Configuration of the CMA-based CP octagonal-ring slot antenna array with sequentially-rotated feed network: (a) front view, (b) rear view.

TABLE 2. Parameters and optimal dimensions of the CMA-based CP octagonal-ring slot antenna array with sequentially-rotated feed network.

Parameters	W_{sub}	R	R_{oa}	R_{ia}	W_d	L_d	θ_c
Values (mm)	120	10	17.5	4	1.5	7.5	30°
Parameters	L_h	R_{oh}	L_a	W_1	W_2	W_3	W_4
Values (mm)	17	24	20	3	1.2	2.5	1.2
Parameters	W_5	W_6	W_7	W_8	h		
Values (mm)	2	1.5	1.5	1.7	1.6		

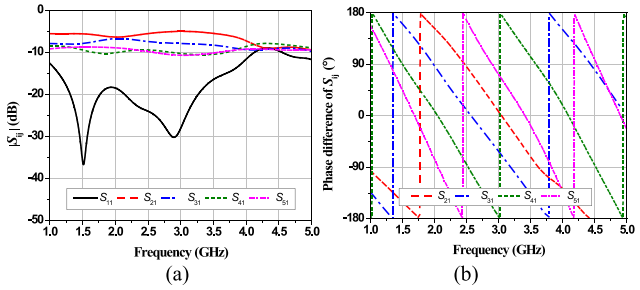

FIGURE 31. Simulated results of the sequentially-rotated feed network: (a) $|S_{ij}|$, (b) phase difference of S_{ij}.

dimensions of the proposed CMA-based CP octagonal-ring slot antenna array with sequentially-rotated feed network.

Figure 31(a) shows the magnitude ($|S_{ij}|$) of the input port (Port 1) and that of the output ports 1 – 5 ($|S_{21}|$, $|S_{31}|$, $|S_{41}|$, and $|S_{51}|$), and Figure 31(b) depicts the phase difference of S_{ij} between output ports. In Figure 31(a), $|S_{11}|$ of Port 1 is below -10 dB between 2 – 4 GHz, while S_{ij} of Ports 2 – 5 are between −5 dB and −11 dB between 2 – 4 GHz. In Figure 31(b), the phase difference between output ports between 2 – 4 GHz are approximately 90°.

Figures 32(a)-(b) show the simulated IBW ($|S_{11}| \leq -10$ dB) and ARBW (AR $\leq$ 3 dB) of the proposed CMA-based CP octagonal-ring slot antenna array with sequentially-rotated feed network. In Figure 32(a), the simulated IBW is 90.41% (1.83 – 4 GHz) at the center frequency of 2.4 GHz. In Figure 32(b), the simulated ARBW at 2.4 GHz is 85% (1.96 – 4 GHz), with the maximum gain of 7.9 dBic at 3.4 GHz.

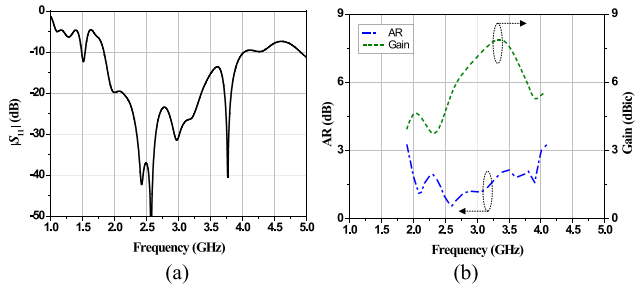

FIGURE 32. Simulated results of the proposed CMA-based CP octagonal-ring slot antenna array with sequentially-rotated feed network: (a) IBW, (b) ARBW and gain.

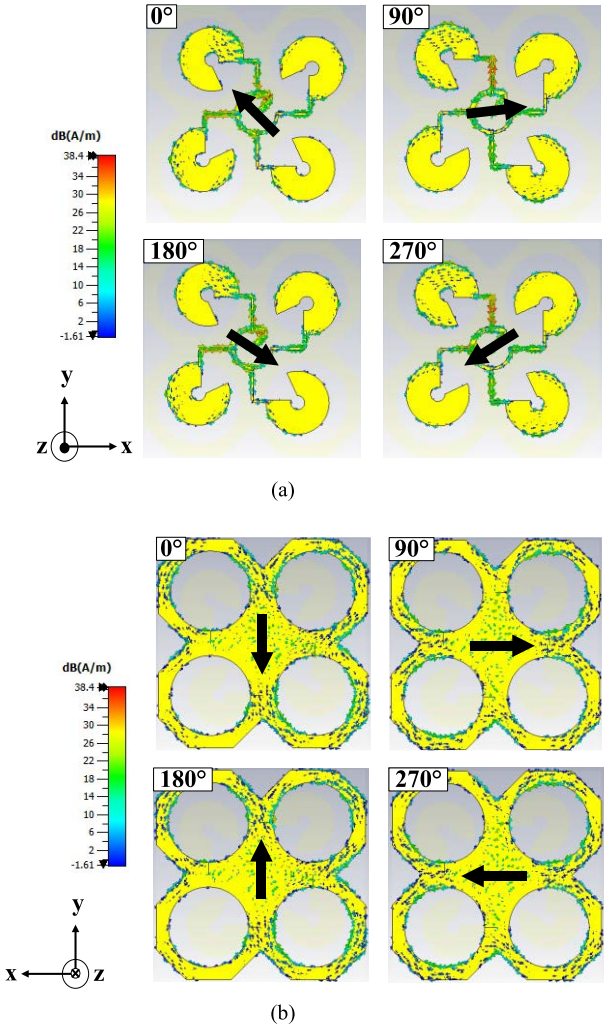

FIGURE 33. Surface current distribution of the CMA-based CP octagonal-ring slot antenna array with sequentially-rotated feed network at 2.4 GHz: (a) upper layer, (b) lower layer.

Figures 33(a)-(b) respectively show the surface current distribution at the center frequency of 2.4 GHz corresponding to phases 0°, 90°, 180°, and 270° on the upper and lower layers of the CMA-based CP octagonal-ring slot antenna array with sequentially-rotated feed network. In Figure 33(a),

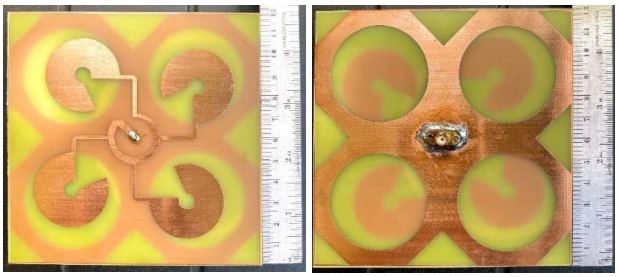

(a) (b)

FIGURE 34. Antenna prototype of the CMA-based CP octagonal-ring slot antenna array with sequentially-rotated feed network: (a) front view, (b) rear view.

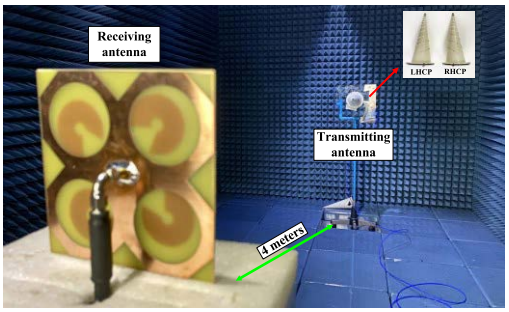

FIGURE 35. Experimental setup of the CMA-based CP octagonal-ring slot antenna array with sequentially-rotated feed network.

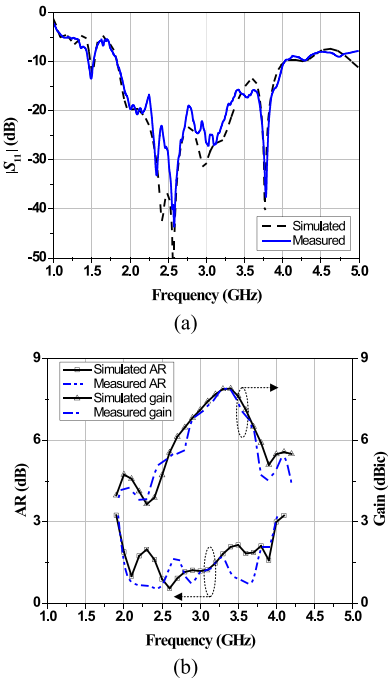

FIGURE 36. Simulated and measured results of the CMA-based CP octagonal-ring slot antenna array with sequentially-rotated feed network: (a) IBW, (b) ARBW and gain.

the electric field vectors on the upper layer travel clockwise in the +z direction, resulting in right-hand circular polarization (RHCP). Meanwhile, the electric field vectors on the lower layer travel counterclockwise in the -z direction, giving rise to left-hand circular polarization (LHCP). As a result, the CMA-based CP octagonal-ring slot antenna array with sequentially-rotated feed network is of bidirectional CP radiation.

V. EXPERIMENTAL RESULTS

Figures 34(a)-(b) depict the front and rear of a prototype of the CMA-based CP octagonal-ring slot antenna array with sequentially-rotated feed network. The experiments were carried out in an anechoic chamber using a vector network analyzer (Rohde&Schwarz ZNLE6 model), as shown in Figure 35. A pair of transmitting antennas (ETS-Lindgren Model 3102 Series Conical Log Spiral antennas) were used to verify the RHCP and LHCP radiations of the antenna prototype (i.e., the receiving antenna). The far-field distance [37] between the transmitting and receiving antennas was 4 m.

To measure the AR of the antenna prototype, the co-polarization (co-pol) and cross-polarization (cross-pol) of electric fields are determined. The co-pol and cross-pol electric fields between the transmitting and receiving antennas correspond to $|E_{co-pol}|$ and $|E_{cross-pol}|$. In other words, the co-pol and cross-pol radiation correspond to RHCP and LHCP radiations. The AR is determined by equation (6) [38].

$$AR(dB) = 20\log\left(\frac{|E_{co-pol}| + |E_{cross-pol}|}{|E_{co-pol}| - |E_{cross-pol}|}\right) \quad (6)$$

where $|E_{co-pol}|$ and $|E_{cross-pol}|$ are the electric field magnitudes of the co- and cross-pol between the transmitting and receiving antennas.

Figures 36(a)-(b) compare the simulated and measured IBW, ARBW and gain of the CMA-based CP octagonal-ring slot antenna array with sequentially-rotated feed network. The simulated IBW ($|S_{11}| \leq -10$ dB), ARBW (AR ≤ 3 dB), and maximum gain are 91.25% (1.83 – 4.02 GHz), 85% (1.96 – 4 GHz), and 7.89 dBic at 3.4 GHz. The measured IBW, ARBW, and maximum gain are 91.6% (1.8 – 4 GHz), 84.5% (1.97 – 4 GHz), and 7.8 dBic at 3.3 GHz. The simulated and measured results are agreeable.

Figures 37(a)-(c) show the simulated and measured RHCP and LHCP radiation patterns in the xz- and yz-planes of the CMA-based CP octagonal-ring slot antenna array with sequentially-rotated feed network at 2, 2.4, and 3.8 GHz, respectively. The simulated and measured RHCP and LHCP are in good agreement.

Table 3 compares the existing CP antenna arrays and the proposed CMA-based CP octagonal-ring slot antenna array with sequentially-rotated feed network in terms of IBW, ARBW, maximum gain, operating frequency bands, and electrical dimension. In [39], a 2 × 2 MTS-based CP stacked patch antenna array (without airgap) with sequentially-rotated feed network suffers from high complexity and

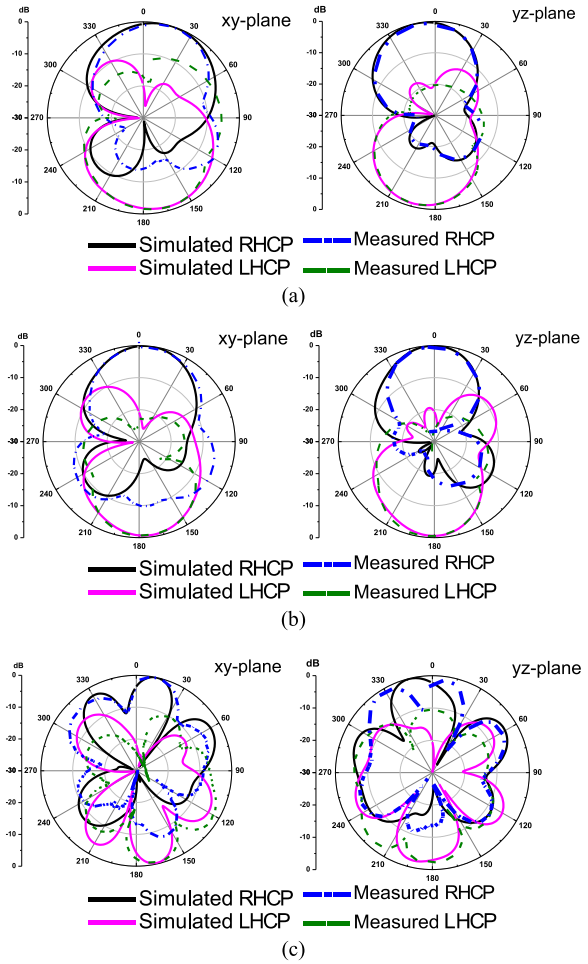

FIGURE 37. Simulated and measured RHCP and LHCP radiation patterns at: (a) 2 GHz, (b) 2.4 GHz, (c) 3.8 GHz.

TABLE 3. Comparison between existing CP antenna arrays and the proposed CMA-based CP octagonal-ring slot antenna array with sequentially-rotated feed network.

Ref.	f_c (GHz)	IBW (%)	ARBW (%)	Maximum gain (dBic)	Electrical dimension at λ_L
[39]	5.5	55.6	41.6	12.08	1.26×1.26×0.05
[40]	5.4	15.9	11.8	12.50	1.45×1.45×0.03
[41]	5.9	43.2	26.5	8.50	0.88×0.88×0.12
[42]	3.1	37.0	37.0	7.50	1.56×1.56×0.02
[43]	2.5	41.0	41.0	8.80	0.83×0.83×0.06
This work	**2.4**	**91.6**	**84.5**	**7.80**	**0.73×0.73×0.01**

f_c is the center frequency of the CMA-based CP planar antennas; and λ_L is the free-space wavelength corresponding to the lowest operating frequency.

bulkiness despite high gain. In [40], a CP 2 × 2 patch with parasitic rectangle antenna array with sequentially-rotated feed network suffers from narrow IBW, ARBW, and bulkiness despite high gain. In [41], a CP stack patch antenna array (with airgap) with double-layer substrates and perpendicular patch at the corners of the ground plane suffers from high complexity. In [42], a 2 × 2 CP patch antenna array with sequentially-rotated feed network suffers from very narrow IBW, ARBW and bulkiness. In [43], a CP stacked patch antenna array with novel sequentially-rotated feed network encounters complex feed network in spite of the low-profile structure. Although the proposed antenna schemes in [42] and [43] achieved wide IBW and ARBW, they fail to cover the entire S-band spectrum (2 – 4 GHz). In comparison, the proposed CMA-based CP octagonal-ring slot antenna array with sequentially-rotated feed network achieves wide IBW of 91.6% (1.8 – 4 GHz) and ARBW of 84.5% (1.97 – 4 GHz), with low-profile and low-complexity structure.

VI. CONCLUSION

This research proposes a low-profile and low-complexity four-element CP octagonal-ring slot antenna array with sequentially-rotated feed network for S-band satellite applications. The proposed antenna array is realized by using an FR-4 substrate and is characterized by CMA. The upper layer of the substrate contains 2 × 2 C-shaped monopoles connected by a sequentially-rotated feed network, and the lower layer of the substrate consists of 2 × 2 octagonal-ring slot ground planes. The four-element octagonal-ring slot antenna array is adopted to improve the CP bandwidth; and the sequentially-rotated feed network to achieve impedance matching. The CMA results indicates that the surface current on the C-shaped monopole of Mode 1 and Mode 2 at 3.2 GHz are orthogonal, while the octagonal-ring slot ground plane generates three pairs of the orthogonal current between Modes 2&5, 3&6, and 1&6 at 1.83, 2.77, and 2.9 GHz. The proposed four-element CP octagonal-ring slot antenna array with sequentially-rotated feed network was simulated using CST Microwave Studio Suite, and an antenna prototype was fabricated and experiments undertaken. The simulated IBW ($|S_{11}| \leq -10$ dB) and ARBW (AR ≤ 3 dB) are 91.25% (1.83 – 4.02 GHz) and 85% (1.96 – 4 GHz), with the maximum gain of 7.89 dBic at 3.4 GHz. Meanwhile, the measured IBW, ARBW, and maximum gain are 91.6% (1.8 – 4 GHz), 84.5% (1.97 – 4 GHz), and 7.8 dBic at 3.3 GHz. Besides, the simulated and measured RHCP and LHCP radiation patterns are in good agreement. Essentially, the proposed antenna scheme is operationally suitable for S-band satellite applications. In addition, this work is the first to characterize the circular polarization of the octagonal-ring slot antenna array using CMA; and to enhance the IBW, ARBW, and antenna gain using the sequentially-rotated feed network. The proposed antenna scheme is also of lower profile, vis-à-vis the existing CP antenna arrays for the S-band spectrum.

REFERENCES

[1] S. Gao, Y. Rahmat-Samii, R. E. Hodges, and X. X. Yang, "Advanced antennas for small satellites," *Proc. IEEE*, vol. 106, no. 3, pp. 391–403, Mar. 2018.
[2] N. Chahat, *CubeSat Antenna Design*. Hoboken, NJ, USA: Wiley, 2021.
[3] S. Liu, P. I. Theoharis, R. Raad, F. Tubbal, A. Theoharis, S. Iranmanesh, S. Abulgasem, M. U. A. Khan, and L. Matekovits, "A survey on CubeSat missions and their antenna designs," *Electronics*, vol. 11, no. 13, p. 2021, Jun. 2022.

[4] S. Li, S. Liao, Y. Yang, W. Che, and Q. Xue, "Low-profile circularly polarized isoflux beam antenna array based on annular aperture elements for CubeSat earth coverage applications," *IEEE Trans. Antennas Propag.*, vol. 69, no. 9, pp. 5489–5502, Sep. 2021.

[5] V. Manohar, S. Bhardwaj, S. B. Venkatakrishnan, and J. L. Volakis, "VHF/UHF ultrawideband tightly coupled dipole array for CubeSats," *IEEE Open J. Antennas Propag.*, vol. 2, pp. 702–708, 2021.

[6] S. Abulgasem, F. Tubbal, R. Raad, P. I. Theoharis, S. Lu, and S. Iranmanesh, "Antenna designs for CubeSats: A review," *IEEE Access*, vol. 9, pp. 45289–45324, 2021.

[7] K. Ramahatla, M. Mosalaosi, A. Yahya, and B. Basutli, "Multiband reconfigurable antennas for 5G wireless and CubeSat applications: A review," *IEEE Access*, vol. 10, pp. 40910–40931, 2022.

[8] V. Rastinasab and H. Weidong, "Implementation and design of RF-front-end telemetry tracking and command subsystem of a CubeSat with 500-km altitude," *IEEE J. Miniaturization Air Space Syst.*, vol. 2, no. 1, pp. 43–47, Mar. 2021.

[9] N. Supreeyatitikul, A. Boonpoonga, and C. Phongcharoenpanich, "Z-shaped metasurface-based wideband circularly polarized Fabry–Pérot antenna for C-band satellite technology," *IEEE Access*, vol. 10, pp. 59428–59441, 2022.

[10] K. Pookkapund, A. Sakonkanapong, R. Kuse, C. Phongcharoenpanich, and T. Fukusako, "Broadband circularly polarized microstrip patch antenna using circular artificial ground structure and meandering probe," *IEEE Access*, vol. 8, pp. 173854–173864, 2020.

[11] P. Janpangngern, D. Torrungrueng, M. Krairiksh, and C. Phongcharoenpanich, "Dual-band circularly polarized omni-directional biconical antenna with double-circular parallelepiped elements for WLAN applications," *IEEE Access*, vol. 10, pp. 31970–31980, 2022.

[12] N. Supreeyatitikul, T. Lertwiriyaprapa, and C. Phongcharoenpanich, "S-shaped metasurface-based wideband circularly polarized patch antenna for C-band applications," *IEEE Access*, vol. 9, pp. 23944–23955, 2021.

[13] F. A. Dicandia and S. Genovesi, "A compact CubeSat antenna with beam-steering capability and polarization agility: Characteristic modes theory for breakthrough antenna design," *IEEE Antennas Propag. Mag.*, vol. 62, no. 4, pp. 82–93, Aug. 2020.

[14] R. Xu, Z. Shen, and S. S. Gao, "Compact-size ultra-wideband circularly polarized antenna with stable gain and radiation pattern," *IEEE Trans. Antennas Propag.*, vol. 70, no. 2, pp. 943–952, Feb. 2022.

[15] R. Xu, S. S. Gao, J. Liu, J. Y. Li, Q. Luo, W. Hu, L. Wen, X. X. Yang, and J. T. S. Sumantyo, "Analysis and design of ultrawideband circularly polarized antenna and array," *IEEE Trans. Antennas Propag.*, vol. 68, no. 12, pp. 7842–7853, Dec. 2020.

[16] N.-W. Liu, L. Zhu, Z.-X. Liu, M. Li, G. Fu, and Y. Liu, "A novel low-profile circularly polarized diversity patch antenna with extremely small spacing, reduced size, and low mutual coupling," *IEEE Trans. Antennas Propag.*, vol. 70, no. 1, pp. 135–144, Jan. 2022.

[17] M. Han and W. Dou, "Compact clock-shaped broadband circularly polarized antenna based on characteristic mode analysis," *IEEE Access*, vol. 7, pp. 159952–159959, 2019.

[18] J. Zeng, X. Liang, L. He, F. Guan, F. H. Lin, and J. Zi, "Single-fed triple-mode wideband circularly polarized microstrip antennas using characteristic mode analysis," *IEEE Trans. Antennas Propag.*, vol. 70, no. 2, pp. 846–855, Feb. 2022.

[19] Y. Chen, X. Li, Z. Qi, H. Zhu, and S. Zhao, "A single-feed circularly polarized loop antenna using characteristic mode analysis," *Int. J. RF Microw. Comput.-Aided Eng.*, vol. 31, no. 7, pp. 1–10, Apr. 2021.

[20] V. S. Bhaskar and E. L. Tan, "Same-sense circularly polarized grid-slotted patch antenna with wide axial ratio bandwidth," *IEEE Trans. Antennas Propag.*, vol. 70, no. 2, pp. 1494–1498, Feb. 2022.

[21] C. Zhao and C. F. Wang, "Characteristic mode design of wide band circularly polarized patch antenna consisting of H-shaped unit cells," *IEEE Access*, vol. 6, pp. 25292–25299, 2018.

[22] F. A. Dicandia and S. Genovesi, "Characteristic modes analysis of non-uniform metasurface superstrate for nanosatellite antenna design," *IEEE Access*, vol. 8, pp. 176050–176061, 2020.

[23] X. Gao, G. Tian, Z. Shou, and S. Li, "A low-profile broadband circularly polarized patch antenna based on characteristic mode analysis," *IEEE Antennas Wireless Propag. Lett.*, vol. 20, no. 2, pp. 214–218, Feb. 2021.

[24] H. H. Tran, N. Nguyen-Trong, and A. M. Abbosh, "Simple design procedure of a broadband circularly polarized slot monopole antenna assisted by characteristic mode analysis," *IEEE Access*, vol. 6, pp. 78386–78393, 2018.

[25] A. Sharma, D. Gangwar, R. P. Singh, R. Solanki, S. Rajpoot, B. K. Kanaujia, S. P. Singh, and A. Lay-Ekuakille, "Design of compact wideband circularly polarized hexagon-shaped antenna using characteristics mode analysis," *IEEE Trans. Instrum. Meas.*, vol. 70, pp. 1–8, 2021.

[26] Y. Chen and C. F. Wang, "Characteristic-mode-based improvement of circularly polarized U-slot and E-shaped patch antennas," *IEEE Antennas Wireless Propag. Lett.*, vol. 11, pp. 1474–1477, 2012.

[27] R. F. Harrington and J. R. Mautz, "Theory of characteristic modes for conducting bodies," *IEEE Trans. Antennas Propag.*, vol. AP-19, no. 5, pp. 622–628, Sep. 1971.

[28] B. B. Q. Elias, P. J. Soh, A. A. Al-Hadi, P. Akkaraekthalin, and G. A. E. Vandenbosch, "A review of antenna analysis using characteristic modes," *IEEE Access*, vol. 9, pp. 98833–98862, 2021.

[29] D.-L. Wen, Y. Hao, H.-Y. Wang, and H. Zhou, "Design of a wideband antenna with stable omnidirectional radiation pattern using the theory of characteristic modes," *IEEE Trans. Antennas Propag.*, vol. 65, no. 5, pp. 2671–2676, May 2017.

[30] Y. Chen and C. -F. Wang, *Characteristic Modes: Theory and Application to Antenna Engineering*. Hoboken, NJ, USA: Wiley, 2015.

[31] A. Abdelaziz, H. A. Mohamed, and E. K. I. Hamad, "Applying characteristic mode analysis to systematically design of 5G logarithmic spiral MIMO patch antenna," *IEEE Access*, vol. 9, pp. 156566–156580, 2021.

[32] A. D. Eva, M. Fabres, M. Ferrando-Bataller, and V. M. R. Penarrocha, "Modal analysis and design of band-notched UWB planar monopole antennas," *IEEE Trans. Antennas Propag.*, vol. 58, no. 5, pp. 1457–1467, May 2010.

[33] B. Feng, X. He, J. Cheng, and C. Sim, "Dual-wideband dual-polarized metasurface antenna array for the 5G millimeter wave communications based on characteristic mode theory," *IEEE Access*, vol. 8, pp. 21589–21601, 2020.

[34] E. H. Newman, "Small antenna location synthesis using characteristic modes," *IEEE Trans. Antennas Propag.*, vol. AP-27, no. 4, pp. 530–531, Jul. 1979.

[35] K. Ding, C. Gao, T. Yu, and D. Qu, "Broadband C-shaped circularly polarized monopole antenna," *IEEE Trans. Antennas Propag.*, vol. 63, no. 2, pp. 785–790, Feb. 2015.

[36] N. Supreeyatitikul, D. Torrungrueng, and C. Phongcharoenpanich, "Quadri-cluster broadband circularly-polarized sequentially-rotated metasurface-based antenna array for C-band satellite communications," *IEEE Access*, vol. 9, pp. 67015–67027, 2021.

[37] C. A. Balanis, *Antenna Theory Analysis and Design*, 3rd ed. Hoboken, NJ, USA: Wiley, 2005.

[38] A. Sakonkanapong and C. Phongcharoenpanich, "Near-field HF-RFID and CMA-based circularly polarized far-field UHF-RFID integrated tag antenna," *Int. J. Antennas Propag.*, vol. 2020, pp. 1–15, Apr. 2020.

[39] S. X. Ta and I. Park, "Compact wideband circularly polarized patch antenna array using metasurface," *IEEE Antennas Wireless Propag. Lett.*, vol. 16, pp. 1932–1936, 2017.

[40] K. Ding, C. Gao, T. Yu, D. Qu, and B. Zhang, "Gain-improved broadband circularly polarized antenna array with parasitic patches," *IEEE Antennas Wireless Propag. Lett.*, vol. 16, pp. 1468–1471, 2017.

[41] K. Ding, Y. Wu, K.-H. Wen, D.-L. Wu, and J.-F. Li, "A stacked patch antenna with broadband circular polarization and flat gains," *IEEE Access*, vol. 9, pp. 30275–30282, 2021.

[42] M. H. Rasekhmanesh, A. Piroutiniya, and P. Mohammadi, "Wideband and low RCS planar circularly polarized array based on polarization conversion of metasurface," *Microw. Opt. Technol. Lett.*, vol. 59, no. 11, pp. 2806–2812, Aug. 2017.

[43] H. Wang, Y. B. Park, and I. Park, "Low-profile wideband solar-cell-integrated circularly polarized CubeSat antenna for the internet of space things," *IEEE Access*, vol. 10, pp. 61451–61462, 2022.

NATHAPAT SUPREEYATITIKUL received the B.Eng. degree from Mahidol University, Thailand, in 2014, the M.Eng. degree from the King Mongkut's University of Technology Thonburi (KMUTT), Thailand, in 2016, and the D.Eng. degree from the King Mongkut's Institute of Technology Ladkrabang (KMITL), Thailand, in 2022. His research interests include circularly polarized antennas and MIMO antennas.

TITIPONG LERTWIRIYAPRAPA (Senior Member, IEEE) received the B.S. (Tech.) (Ed.) degree in electrical engineering from the King Mongkut's University of Technology North Bangkok, in 1996, the M.Eng. degree in electrical engineering from the King Mongkut's Institute of Technology Ladkrabang, in 2000, and the M.Sc. and Ph.D. degrees in electrical engineering from The Ohio State University, Columbus, OH, USA, in 2006 and 2007, respectively. He is currently an Associate Professor with the Department of Teacher Training in Electrical Engineering, King Mongkut's University of Technology North Bangkok. His research interests include electromagnetic theory, metamaterial, asymptotic, computational electromagnetics, and hybrid methods. He received the third place in the 2007 USNC/CNC URSI Student Paper Competition, held in Ottawa, Canada, and the Best Paper Award from the 2008 International Symposium on Antennas and Propagation (ISAP2008), Taiwan. He was with the Board Committee of the ECTI Association, from 2012 to 2015.

MONAI KRAIRIKSH (Senior Member, IEEE) was born in Bangkok, Thailand. He received the B.Eng., M.Eng., and D.Eng. degrees in electrical engineering from the King Mongkut's Institute of Technology Ladkrabang (KMITL), Thailand, in 1981, 1984, and 1994, respectively. He was a Visiting Research Scholar at Tokai University, in 1988, and the Yokosuka Radio Communications Research Center, Communications Research Laboratory (CRL), in 2004. He worked as the Director of the Research Center for Communications and Information Technology, from 1997 to 2002. He joined the KMITL and currently a Professor at the Department of Telecommunication Engineering. His research interests include antennas for wireless communications and microwave in agricultural applications. He was the Chairperson of the IEEE MTT/AP/Ed Joint Chapter, in 2005 and 2006. He served as the General Chairperson of the 2007 Asia–Pacific Microwave Conference and the Advisory Committee of the 2009 International Symposium on Antennas and Propagation. He was the President of the Electrical Engineering/Electronics, Computer, Telecommunications and Information Technology Association (ECTI), in 2010 and 2011, and the Editor-in-Chief of the *ECTI Transactions on Electrical Engineering, Electronics, and Communications*. He was recognized as a Senior Research Scholar of the Thailand Research Fund, in 2005 and 2008, and a Distinguished Research Scholar of the National Research Council of Thailand. He served as a Distinguished Lecturer for the IEEE Antennas and Propagation Society, from 2012 to 2014.

CHUWONG PHONGCHAROENPANICH (Member, IEEE) received the B.Eng. (Hons.), M.Eng., and D.Eng. degrees from the King Mongkut's Institute of Technology Ladkrabang (KMITL), Bangkok, Thailand, in 1996, 1998, and 2001, respectively. He is currently a Professor with the Department of Telecommunications Engineering, KMITL, where he also works as the Leader of the Innovative Antenna and Electromagnetic Applications Research Laboratory. His research interests include antenna design for various mobile and wireless communications, conformal antennas, and array antenna theory. He is also a Senior Member of IEICE and a member of ECTI. He has served as the Chair of the IEEE MTT/AP/ED Thailand Chapter, from 2014 to 2018. He has been on an Organizing Committee of several international conferences, including the TPC Chair of 2009 International Symposium on Antennas and Propagation (ISAP 2009) and a TPC Member of ISAP 2012. He is also a Reviewer of many scientific journals, including the IEEE TRANSACTIONS ON ANTENNAS AND PROPAGATION, IEEE ACCESS, *IET Microwaves, Antennas and Propagation*, *Electronics Letters*, and *ECTI Transactions*, and many international conferences, including ISAP and APMC. He was on the Board Committee of ECTI Association, from 2008 to 2011 and from 2014 to 2015. He was an Associate Editor of the *IEICE Transactions on Communications* and the *ECTI Transactions on Electrical Engineering, Electronics, and Communications*. He is also an Associate Editor of the *IEICE Communications Express*.